© 2018 IEEE. Personal use of this material is permitted. Permission from IEEE must be obtained for all other uses, in any current or future media, including reprinting/republishing this material for advertising or promotional purposes, creating new collective works, for resale or redistribution to servers or lists, or reuse of any copyrighted component of this work in other works.

3D Granulometry Using Image Processing

R. Donida Labati, A. Genovese, E. Muñoz, V. Piuri, *Fellow, IEEE,* and F. Scotti, *Senior Member, IEEE*

***Abstract*—Image-based methods for estimating the particle size distribution (granulometry) usually analyze two-dimensional (2D) samples of particles disposed on a conveyor belt. Such approaches have to deal with occlusions and cannot evaluate the thickness of each particle. Three-dimensional (3D) vision systems can reduce the acquisition constraints and speed up the quality control process. This paper proposes a novel 3D vision system for analyzing the granulometry of falling particles. The system is designed to work in real-time and to compute a partial 3D reconstruction of the particle from a single pair of two-view images, which is then enhanced by using a neural-based technique. The validation of the proposed approach has been performed by considering three application scenarios for which the system achieved satisfactory accuracy and robustness.**

***Index Terms*—Granulometry, 3D reconstruction, image processing, falling particles**

I. Introduction

Granulometry, also known as particle size distribution, can be defined as "a description of the size and frequency of particles in a population" [1]. The granulometry of materials is relevant in a wide range of applications, such as pharmaceutical production, food processing, paper making, textile fabrication, coating manufacturing, or modeling geological processes, because the properties of the final product or the observed phenomenon depend on the shapes and sizes of the particles [2], [3], [4], [5].

To determine the actual sizes and provide effective, automatic, inline, and contactless procedures, computer vision systems can analyze the images of the particles while they are transported [6]. The majority of these methods analyze images from particles laying on a conveyor belt. This configuration can use a simple acquisition setup, but it presents four important drawbacks. First, especially in the case of thin and flat particles, measuring the thickness of each particle is difficult or impossible since the objects to be analyzed are usually oriented parallel to the conveyor surface. Second, the particles tend to occlude or touch each other, thus, increasing the complexity of the segmentation. Third, this configuration permits to observe only the topmost particles because smaller particles tend to remain at the bottom layer of material. Fourth, the particles are usually deposed densely and are much more difficult to detect and segment with respect to falling particles because frequently the particles have uniform color and overlap or touch each other [7].

A possible solution to the aforementioned problems is to analyze the particles by performing a single two-view acquisition while they are falling, thus being able to analyze three-dimensional (3D) characteristics. This approach has the following advantages. First, falling particles can present their thickness oriented towards the camera, thus permitting to perform accurate measurements. Second, it is possible to capture particles in any orientation by exploiting the random rotations of falling particles, thus providing the means to analyze all the three dimensions of the particles with a single acquisition setup. Third, falling particles are less prone to occlusions with respect to images of material disposed on conveyor belt [8]. Fourth, in the case of separated falling particles, it is possible to segment them without requiring texture-specific information, for example by using general histogram-based or edge-based segmentation techniques.

The authors are with the Department of Computer Science, Università degli Studi di Milano, via Bramante 65, I-26013 Crema (CR), Italy, e-mail: {*firstname.lastname*}@unimi.it

Table I
NOTATIONS AND PARAMETERS USED IN THIS PAPER

Notation	Description
CI	Computational Intelligence
ROI	Region of Interest
HSV	Image color representation based on Hue (H), Saturation (S), and Value (V)
YUV	Image color representation based on luma (Y) and chrominance (UV)
Sobel operator	Discrete differentiation operator that approximates the gradient of the image intensity function [9]
8-connected component	Cluster of pixels in an image with the same value, connected through each other 8-connectivity. The 8-connectivity of a pixel p at location (x, y) includes the locations $(x+1, y)$, $(x-1, y)$, $(x, y+1)$, $(x, y-1)$, $(x+1, y+1)$, $(x+1, y-1)$, $(x-1, y+1)$, $(x-1, y-1)$ [9]
Cubic spline	An approximation function of piecewise third-order polynomials passing through a set of control points [10]
$\lvert \cdot \rvert$	Cardinality of the set
$\overline{\mathbf{a}}, \sigma(\mathbf{a})$	Mean and standard deviation of vector $\mathbf{a}$
l, w, t	Length, width, and thickness of the particle
$\hat{l}'$, $\hat{w}'$, $\hat{t}'$	Preliminary estimations of l, w, t
$\hat{l}$, $\hat{w}$, $\hat{t}$	Final estimations of l, w, t
Camera$_A$, Camera$_B$	Cameras used in the proposed setup
I_A, I_B	Images captured using Camera$_A$ and Camera$_B$
u, v	Width and height of I_A, I_B
R_A, R_B	ROIs of I_A, I_B
E_A, E_B	Enhanced images
E'_B, R'_B	E_B and R_B after correcting perspective distortions
r, c	Row and column indexes of an image
α_C	Orientation difference between Camera$_A$ and Camera$_B$
β	Yaw orientation of the particle with regard to Camera$_A$
θ	Roll orientation of the particle, defined as the angle between the y axis and the major axis of the ellipse fitting the particle shape in the binary image R_A
H	Homography matrix
th_s	Threshold used to binarize I_A and I_B
th_{Area}	Threshold used to discard 8-connected components with insufficient area to represent a particle
th_c	Threshold used to detect overlapping particles
$t_{frontal}$, $t_{sideways}$	Thresholds used to determine if a particle has been captured with a frontal or sideways orientation, by analyzing its yaw orientation
t_p	Threshold used to discard outliers in the 3D point cloud of the particle, representing the maximum distance of every point from an approximating plane representing the 3D surface to which it pertains

In industrial applications, particulate materials are often let fall during their handling. However, the acquisition and analysis of images in this environment is more complex than on the conveyor belt because the particles fall faster, with uncontrolled movements and the acquired images can contain objects with random rotations on the three axes. A 3D acquisition system based on a two-view setup, as the one proposed in this paper, can provide the following advantages. First, a 3D reconstruction can compute a model invariant to the position and orientation of the particle. Second, a metric 3D representation, achieved using a calibrated acquisition system, permits to estimate the real size of the particle in an unconstrained falling space.

This paper proposes a novel vision system for the granulometric analysis of falling particles, which is based on two-view acquisitions, 3D reconstruction, and Computational Intelligence (CI). The main scope of this system is the granulometric estimation of the length (l), width (w) and thickness (t) of each single particle to subsequently obtain the characteristic parameters of the particle size distribution, such as the mean and standard deviation of l, w, and t. The main contributions of the proposed system are the following: *i*) it can estimate the thickness of small objects, which is not visible in particles deposed on a conveyor belt; *ii*) it alleviates possible problems due to occlusions with respect to state-of-the-art technologies, since falling particles are better separated than those deposed on a conveyor belt; *iii*) it permits to obtain a less biased sampling, because falling particles tend to be distributed more regularly, while on conveyor belts smaller particles tend to remain at the bottom; *iv*) it can perform an inline metric 3D reconstruction and granulometric analysis of falling thin particles using a single two-view acquisition, with a sub-pixel estimation of the thickness; *v*) it is texture independent, hence it can analyze particles of different materials; *vi*) it refines the granulometric analysis by exploiting CI, which, being conceived to work in imperfect and complex domains, such as the production line [11], facilitates the calibration of the system according to the application; *vii*) it is fast and robust, making it suitable for inline applications; *viii*) it uses images obtained using an acquisition setup composed only of two cameras and commercial LED illuminators.

This work focuses on falling lath-, plate- and flake-shaped particles, which are particularly challenging to measure using vision systems. In the literature, the proportions of length, width and thickness are in the following ranges [2]: *lath*: $(10-50) : (2-5) : 1$; *plate*: $\sim 1 : \sim 1 : (0.1-0.6)$; *flake*: $\sim 1 : \sim 1 : < 0.1$.

To the best of our knowledge, this is the first image-based approach in the literature dealing with the 3D measurement of falling particles. Moreover, its results in three case studies show that it is effective, robust to different kinds of materials, and exhibits satisfactory accuracy.

The paper is organized as follows. Section II presents the state of the art. Section III describes the proposed approach. Section IV and V describe the experimental results and conclusions, respectively. Table I presents the list of notations and parameters used in the paper.

II. Previous Work

Currently, the vast majority of granulometry methods based on image processing techniques perform a two-dimensional (2D) analysis, and only a few works perform 3D measurements [12].

In general, 2D systems process images captured using a single camera [13]. The work described in [14] applies successive structural openings of the segmented image, while the one in [15] uses clustering to segment the particles. Other methods are based on the watershed computation [16], edge detection or mathematical morphology processing [17], [3], [18], fuzzy clustering [7], and analysis of images obtained with different illumination conditions [19].

However, in uncontrolled setups, the segmentation step of these methods can be an important source of errors in the estimation of particle sizes [6]. These errors can be particularly relevant when a high number of occlusions occur or when the quality of the illumination is poor. To avoid this problem, researchers have proposed methods that do not rely on segmentation. As illustrated in [20], the analysis of the Fourier transform represents a good alternative. More recent studies have applied techniques such as morphological opening operations [21] or neural networks [6].

Approaches that only analyze 2D images have important disadvantages with respect to methods analyzing 3D models since they can have difficulties dealing with illumination changes or with variations in the intensity and texture of the materials [12]. Considering the approaches based on 2D images, the additional information in color images with respect to grayscale images can help in achieving a more robust segmentation of the particles by considering the color difference between the texture of the material and the background. However, single-camera setups do not permit to easily compensate perspective distortions or easily distinguish individual particles from overlapped particles.

3D scanners [22] have demonstrated their robustness in measurement applications [12]. Nevertheless, this kind of solution requires the use of complex and expensive hardware. Other alternatives studied for granulometry analysis are multi-flash imaging and shape from shading techniques [23]. However, they require complex illumination setups. 3D reconstruction methods based on stereo vision are simpler and require less expensive hardware setups [24]. The work in [25] has successfully applied a multiple view approach to separated samples, while the system in [26] has reconstructed 3D models of particles placed on a conveyor belt.

To increase the accuracy of the granulometric analysis, it is possible to analyze images of particles captured as they fall. In this way, the particles are better separated with respect to traditional setups based on conveyor belts, since the fall increases the speed of the particles and hence their distance from each other. In particular, after falling few centimeters, the speed of the particles is more than the one achievable with most conveyor belts used for separating particles. The work in [8] follows this approach, although it only analyzes 2D images.

To the best of our knowledge, the proposed system is the first study on multiple view and 3D techniques for analyzing

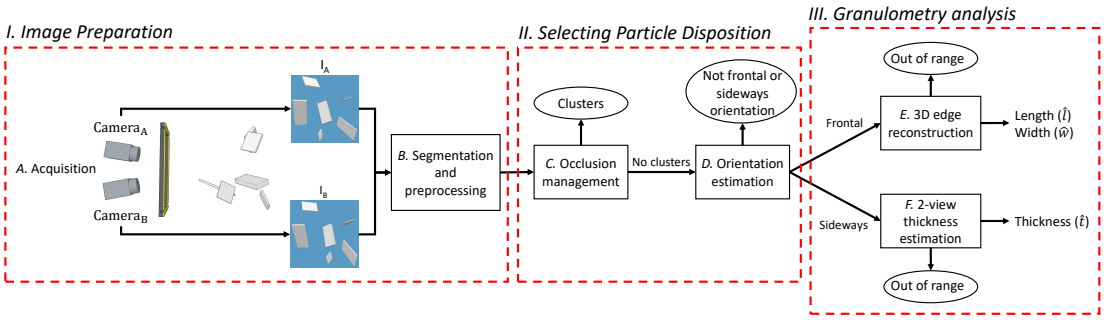

Figure 1. Outline of the proposed vision system. After the segmentation, the occlusion management step discards clusters of overlapping particles. Then, the orientation of the particles is evaluated: the proposed method uses particles with a frontal orientation to estimate the length ($\hat{l}$) and width ($\hat{w}$), and particles with a sideways orientation to estimate the thickness ($\hat{t}$). The main novelties of the proposed system are the innovative methods for selecting the particle disposition (steps C and D) and for the granulometry analysis (steps E and F)

the granulometry of falling particles.

III. The Proposed Approach

The system uses a two-view image acquisition setup, image processing algorithms, 3D reconstruction methods, and CI techniques to obtain the mean and standard deviation of l, w, and t of the particles by performing the granulometric estimation of each single particle. In the rest of the paper, $\hat{l}$, $\hat{w}$, $\hat{t}$ represent the estimated values of l, w, and t using the proposed method. Two-view acquisitions and 3D reconstruction methods are used since they can compute a metric representation of the particles, invariant to their position and orientation with respect to the camera. The metric reconstruction describes the real size of the particles and their actual position in the scene, expressed in millimeters and using a reference system centered in the optical center of a reference camera [27]. The computed 3D models are processed for estimating the particle size measurements, which are refined using CI techniques. CI techniques also permit to easily adapt the granulometry analysis for heterogeneous materials, environments, and application scenarios.

Once the particles are falling, the system performs the following steps: *A*) acquisition, *B*) segmentation and preprocessing, *C*) occlusion management, *D*) orientation estimation, *E*) 3D edge reconstruction, *F*) two-view thickness estimation. The main novelties of the proposed system are the innovative methods for selecting the particle disposition (steps C and D) and for the granulometry analysis (steps E and F). Fig. 1 presents the main modules and steps of the proposed vision system.

A. Acquisition

The acquisition setup uses two calibrated cameras. In particular, the proposed implementation uses two Sony XCD-SX90CR color CCD cameras, synchronized using a trigger mechanism. Fig. 2 shows the schema of the setup. The cameras are positioned horizontally, with an angle $\alpha = 85°$ with respect to the support, and separated by a baseline $\Delta_D = 125$ mm. It has been demonstrated in the literature that increasing the baseline Δ_D enables to reduce the error in estimating the three-dimensional depth information. At the same time, increasing the baseline requires to increase the camera angle α to have the two cameras point at the same area represented by the intersection between the fields of view. However, increasing either Δ_D or α reduces the accuracy of algorithms for

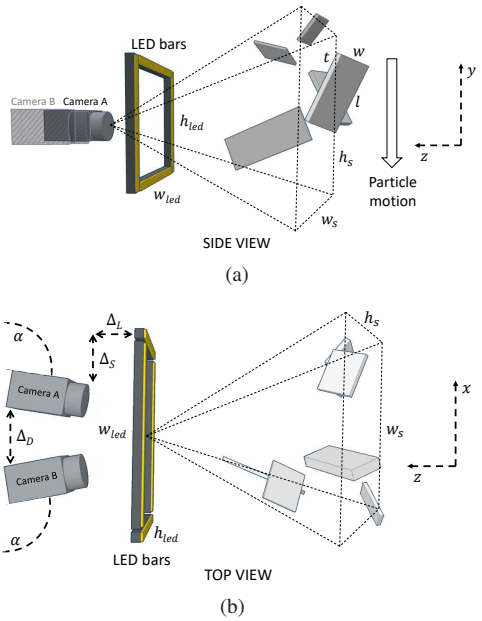

Figure 2. Representation of the used acquisition setup: (a) side view; (b) top view. The direction of the particle motion is along the y axis in the used reference frame

searching for corresponding points in the images captured by the two cameras [28]. The orientation angle α and the baseline Δ_D are then empirically chosen as a trade-off between the error in estimating the three-dimensional depth information and the accuracy in searching for corresponding points.

Four LED bars, with sizes $w_{led} = 400$ mm and $h_{led} = 300$ mm are placed around the cameras with distances $\Delta_L = 90$ mm and $\Delta_S = 90$ mm. The size and distances of the LED bars are chosen to produce a uniform illumination over the fields of view of the cameras, that permits capturing falling particles with a shutter time sufficiently fast to avoid motion blur.

The setup performs a synchronized two-view acquisition when particles are entirely contained in the field of view of both Camera$_A$ and Camera$_B$. A photocell trigger detects the presence of particles and enables real-time acquisitions. The color of the background used for this work is blue, although different background colors permitted to obtain similar results during preliminary tests.

To reconstruct metric 3D models, it is necessary to calibrate the cameras offline by computing their intrinsic and extrinsic

parameters, and the homography matrix H. To do so, this work uses the algorithms described in [27], [29].

B. Segmentation and Preprocessing

This section describes the computation of the region of interest (ROI) of each image, defined as the region representing separated particles or separated groups of overlapping particles. Then, the system enhances the images and applies a rectification step. The proposed method can be divided into three tasks: *i*) segmentation, *ii*) enhancement, *iii*) rectification. Fig. 3 shows a detailed outline of the segmentation and preprocessing step.

1) Segmentation: The proposed segmentation algorithm can cope with several aspects that influence the visibility of the particles, such as the background, light conditions, and differences in orientation, thickness, or color of the evaluated objects. In addition, the algorithm discards image regions representing dust or small particles (e.g., chopped wood strands with length or width less than 2 mm).

The proposed algorithm combines a color-based and an edge-based technique. The former uses the method described in [30] to segment the S channel of the HSV representation of I, obtaining the binary image S_b. The latter reduces the background noise by applying a median filter to the luminance channel Y of the YUV representation of I. The next step consists of applying a Sobel edge detector [9] and binarizing the image using the empirically estimated threshold th_s, obtaining Y_b. The threshold th_s is estimated following the procedure described in Section IV-A. Subsequently, S_b and Y_b are combined by using the OR operator, obtaining the binary ROI image R. The segmentation algorithm then discards the 8-connected components with area lower than an empirically estimated threshold th_{Area}. The threshold th_{Area} is empirically estimated following the procedure described in Section IV-A, which evaluates the size of the particles in the considered application to robustly discard dust and broken particles. The segmentation algorithm is applied to I_A as well as I_B, obtaining the ROIs R_A and R_B, respectively.

2) Enhancement: First, the proposed enhancement algorithm applies a contrast stretching to I and uses the segmentation mask R to discard the regions that do not belong to the particle, obtaining E. After that, it applies the method in [31] to correct the distortions introduced by the lenses in the two-view images. The enhancement algorithm is applied to I_A as well as I_B, obtaining the enhanced images E_A and E_B, respectively.

3) Rectification: This step rectifies E_B to facilitate the 3D reconstruction process, obtaining E'_B, so that the epipolar lines of E'_B are horizontal and correspond to the lines parallel to the x axis of E_A [32]. The rectification procedure computes E'_B using the homography matrix H estimated during the calibration step. Then, the same rectification procedure is applied to R_B, obtaining R'_B.

C. Occlusion Management

The images may contain an arbitrary number of falling particles, with random positions and orientations. Hence, it is necessary to select the particles for which the granulometric analysis is feasible. This work identifies two particle configurations: *1*) separated particles and *2*) overlapping or touching particles.

This section describes a general method based on the shape of each 8-connected component in the segmented image R to discard groups of particles overlapping while falling. Fig. 4 shows a detailed outline of the occlusion management step.

The proposed system determines if the images depict separated or overlapping particles. The system only uses separated particles for the granulometry analysis and discards overlapping particles because, similarly to the case of the particles lying on the conveyor belt, it would not be possible to robustly separate them without using texture information specific for the considered material. Nevertheless, in the case of falling particles, only a fraction of the 8-connected components represents overlapping particles.

The method analyzes the shape of each 8-connected component $i \in R$, by calculating $d_i = a_{convex,i} - a_i$, where $a_{convex,i}$ is the area of the convex hull of i and a_i is its actual area. All components $d \in R$ such that $d_d > th_c$ are considered overlapping particles, and are discarded. The threshold th_c is empirically estimated following the procedure described in Section IV-A and should be tuned according to the application scenario and the shape of the particles. Fig. 5 shows an example of the occlusion management step. In particular, the area difference d_i is not normalized by the area a_i of the component i since the normalized d_i/a_i tends to be greater on smaller particles due to the irregularities of the shape of the particle and would require to take into account the characteristics of the shape of the particle to adjust the threshold th_c. In the proposed approach, since small particles are discarded using the method described in Section III-B, thresholding the non-proportional area difference d_i proved to be effective in detecting occluded particles.

D. Orientation Estimation

The proposed system has the advantage of capturing particles in any orientation by exploiting the random rotations of falling particles, without changing the architecture of the setup. In this way, it is possible to analyze all three dimensions of the particles (l, w, and t) based on the orientation of the particle at the moment of the acquisition. When the system detects a separated particle, it can be captured in three possible orientations: *1a*) frontal, *1b*) sideways, *1c*) and intermediate orientation (not frontal or sideways orientation).

Frontal acquisitions present the surface of the particle oriented approximately perpendicularly to the optical axis of Camera$_A$. The proposed system uses them to estimate the l and w. However, t is not completely visible, especially for thin particles. Differently, sideways samples show particles captured with the surface oriented approximately in parallel to the optical axis of Camera$_A$, exposing their thinner side. The proposed system uses them to estimate t. Samples with intermediate orientation are discarded, because they do not permit to robustly estimate w or t.

To distinguish the three different cases, the orientation estimation module analyzes the orientation difference α_C between the cameras, and the widths of the segmented ROIs.

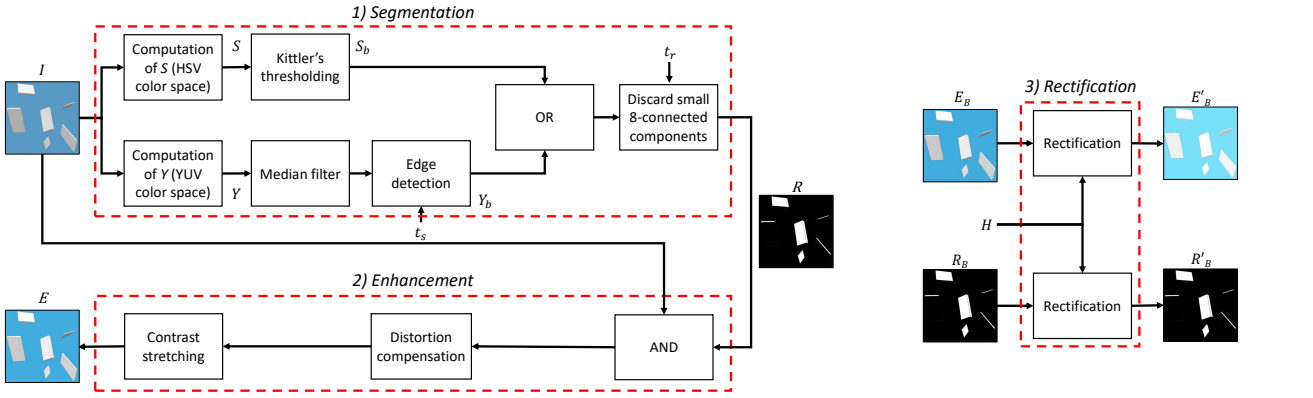

Figure 3. Outline of the segmentation and preprocessing step

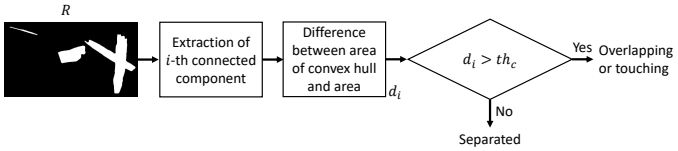

Figure 4. Outline of the occlusion management step

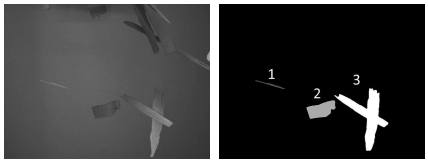

(a) (b)

Figure 5. Example of the output of the occlusion management algorithm applied on raw material particles (chopped wood strands): (a) image I; (b) the ROI image R, containing the 8-connected components describing separated particles (components 1, 2) or separated groups of overlapping particles (component 3)

This method is accurate and computationally efficient since it determines the orientation of the surface of the particle with respect to the cameras without performing a complete 3D reconstruction. Fig. 6 shows a detailed outline of the orientation estimation step.

The method considers a reference system centered in the optical center of Camera$_A$ (Fig. 7). Let w and t be respectively the real width and thickness of a particle captured by the proposed system and β its yaw orientation with regard to Camera$_A$. Camera$_A$ and Camera$_B$ perceive w as $w_A = w\cos(\beta) + t\sin(\beta)$ and $w_B = w\cos(\beta - \alpha_C) + t\sin(\beta - \alpha_C)$, respectively. Since the contribution of t in the computation of w can be considered negligible for thin particles, the equations can be simplified as:

$$\begin{cases} w_A = w\cos(\beta) \\ w_B = w\cos(\beta - \alpha_C) \end{cases} . \quad (1)$$

To provide a more robust estimation, the proposed approach computes $\mathbf{w}_A(r), \mathbf{w}_B(r)$ for each row r by extracting the width of the connected component in R_A, R'_B, respectively, and solves Eq. 1 for each row. Then, it estimates β as the average result. If $\beta < t_{frontal}$, the proposed system considers that the particle has been captured with a frontal orientation, if $\beta > t_{sideways}$, that the particle has been captured with a sideways orientation, and if $t_{frontal} \leq \beta \leq t_{sideways}$, that the particle has been captured with an intermediate orientation, with $t_{frontal} < t_{sideways}$. The thresholds $t_{frontal}$ and $t_{sideways}$ are empirically estimated following the procedure described in Section IV-A. Fig. 8 shows an example of a particle captured in the frontal and sideways orientations.

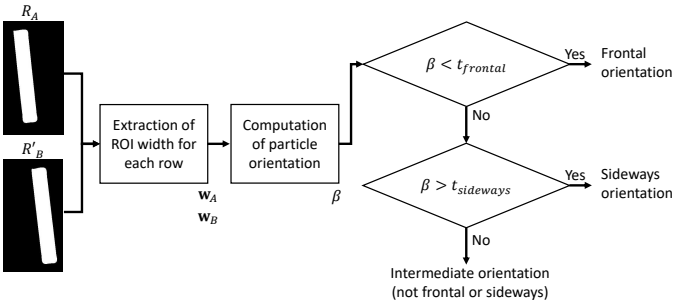

Figure 6. Outline of the orientation estimation step

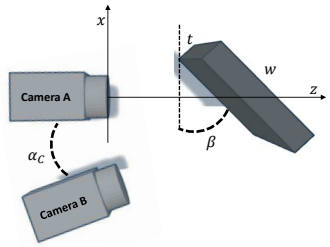

Figure 7. The reference system used to estimate the orientation β: w is captured by Camera$_A$ as $w_A = w\cos(\beta)$, and by Camera$_B$ as $w_B = w\cos(\beta - \alpha_C)$. t is captured by Camera$_A$ as $t_A = t\sin(\beta)$, and by Camera$_B$ as $t_B = t\sin(\beta - \alpha_C)$

E. 3D Edge Reconstruction

This section describes the proposed method for estimating $\hat{l}$ and $\hat{w}$ of falling thin particles by performing the 3D reconstruction of the edges, normalizing the resulting point cloud, estimating the length and width from the point cloud, and using a CI-based enhancement. The method can only operate for particles with a frontal orientation (orientation *1a*), detected using the method described in Section III-D. The proposed method can be divided into four tasks: *i*) edge matching and 3D triangulation, *ii*) 3D normalization, *iii*) length and width estimation, *iv*) CI enhancement. Fig. 9 shows a detailed outline of the 3D edge reconstruction step.

1) Edge Matching and 3D Triangulation: To estimate $\hat{l}$ and $\hat{w}$, it is not necessary to know the details of each surface of the evaluated particle. Therefore, the proposed system does

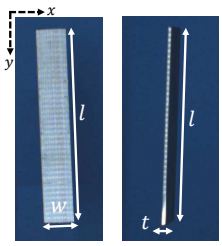

(a) (b)

Figure 8. Example of a particle captured in different orientations using the proposed approach applied on the calibration parallelepipeds case study: (a) particle captured in frontal orientation. It is possible to observe the l and w dimensions of the particle; (b) particle captured in a sideways orientation. It is possible to observe the l and t dimensions of the particle

not compute the 3D position of every point of the particle. Furthermore, by only computing the 3D coordinates of the edges of the particles, the system is fast and invariant to differences in the textures of the considered material. In addition, it is not needed to use complex algorithms for match rejection [33].

To compensate the 2D rotation of the particle, the proposed 3D reconstruction algorithm rotates R_A of $-\theta$ degrees, obtaining $R_{A-\theta}$, and then estimates the angle θ of the roll rotation as the angle between the y axis and the major axis of the ellipse fitting the particle shape in R_A. The same rotation is applied to R'_B, obtaining $R'_{B-\theta}$. To align the two images, the algorithm resizes $R'_{B-\theta}$ so that the ROI spans the same number of rows as in $R_{A-\theta}$.

Then, the algorithm extracts the edges of $R_{A-\theta}$ and $R'_{B-\theta}$ using the Sobel operator and a thresholding step, obtaining the binary images $B_{A-\theta}$ and $B'_{B-\theta}$ and the sets of points $P_{A-\theta}$ and $P_{B-\theta}$. After that, it computes the set $P_{-\theta}$ of pairs of corresponding points as follows:

$$|P_{A-\theta}(j)| = |P_{B-\theta}(j)| \rightarrow (x,j)_A, (x,j)_B \in P_{-\theta}$$
$$(x,j)_A \in P_{A-\theta}(j),\ (x,j)_B \in P_{B-\theta}(j)\ \ \forall\ 1 < j < v\ \ , \quad (2)$$

where $|\cdot|$ represents the cardinality of a set, $P_A(j) \subset P'_A$ and $P_B(j) \subset P'_B$ represent the subsets of points where $y = j$, v is the vertical size of the image, and $P_{-\theta}$ is the set of matched pairs of points.

To obtain the coordinates of the matched points on the images E_A and E'_B, the algorithm reverses the alignment and rotation process and obtains the set of points P.

The z coordinate of each matched pair of points is then computed using the triangulation function [27]:

$$z = (ft_o)/(x_A - x_B)\ \ , \quad (3)$$

where f is the focal length of Camera$_A$ and Camera$_B$, t_o is the translation between the optical centers of the two cameras obtained using the calibration procedure, x_A and x_B are two matched points $\in P$. Fig. 10b shows an example of a 3D point cloud $(\mathbf{x}, \mathbf{y}, \mathbf{z})$.

2) 3D Normalization: To obtain accurate measurements, it is necessary to perform a 3D normalization that removes outliers, compensates for the roll and pitch rotations, and minimizes the displacement along the z axis.

The proposed normalization first applies a linear interpolation to P to obtain a plane $(\mathbf{x}_p, \mathbf{y}_p, \mathbf{z}_p)$. Since thin particles are nearly flat, the algorithm considers as outliers the points with distance to the plane approximating the surface which is greater than a threshold t_p, empirically estimated following the procedure described in Section IV-A.

In addition, the normalization algorithm compensates the rotations of the particle in the 3D space. The displacements of the plane along the three axes can represent the catheti of two right triangles (Fig. 10b), which permit to compute the pitch and roll angles using trigonometric formulas. In particular, the algorithm estimates the roll angle α_{roll} along x and z axes and the pitch angle α_{pitch} along y and z axes. After that, it compensates them using 3D rotation matrices.

Fig. 10c shows an example of the 3D normalization step.

3) Length and Width Estimation: To estimate the length and width of a thin particle, the system first projects the point cloud on a plane, so that it appears as a fully frontal acquisition, obtaining the binary image F. No scaling or warping is performed to guarantee a metric representation.

Then, the proposed algorithm for estimating $\hat{l}$ and $\hat{w}$ computes C as the filled convex hull of F and compensates the rotation as in Section III-E1, obtaining $C_{-\theta}$. To model more accurately the size of the particle, we calculate the points where the major axis of the fitting ellipse Maj_C, its minor axis Min_C, intersect with the edges of the particle, and estimate the preliminary length $\hat{l}'$ and width $\hat{w}'$.

4) CI Enhancement: The proposed system uses neural networks, trained using the procedure described in Section IV-F, to enhance the estimated $\hat{l}'$ and $\hat{w}'$ and obtain the final estimations $\hat{l}$ and $\hat{w}$. The neural network N_l enhances $\hat{l}'$, and the neural network N_w enhances $\hat{w}'$. N_l and N_w use the feature sets F_l and F_w, respectively.

The set F_l is composed of the following features:

$$F_l = \big[\hat{l}'; \hat{l}' \cdot \hat{w}'; Per; (\hat{l}' \cdot \hat{w}')/Per; \hat{l}'/\hat{w}'; \alpha_{roll}; \alpha_{pitch}; \theta; d_0;$$
$$\overline{(h_A(c))}; \sigma_{(h_A(c))}; \overline{(h_B(c))}; \sigma_{(h_B(c))}; Maj_A; Maj_B\big]\ \ , \quad (4)$$

where Per is the perimeter of the particle, d_0 is the distance from the center of the point cloud to the axes origin, $h_A(c)$ and $h_B(c)$ are the height values of the 8-connected components in E_A and E'_B for every column c, Maj_A and Maj_B represent the major axis of the 8-connected components in R_A and R'_B.

Similarly, the set F_w is composed of the following features:

$$F_w = \big[\hat{w}'; \hat{l}' \cdot \hat{w}'; Per; (\hat{l}' \cdot \hat{w}')/Per; \hat{l}'/\hat{w}'; \alpha_{roll}; \alpha_{pitch}; \theta; d_0;$$
$$\overline{(w_A(c))}; \sigma_{(w_A(c))}; \overline{(w_B(c))}; \sigma_{(w_B(c))}; Min_A; Min_B\big]\ \ , \quad (5)$$

where $w_A(c)$ and $w_B(c)$ are the width of the 8-connected components in E_A and E'_B for every column c, Min_A and Min_B are the minor axis of the 8-connected components in R_A and R'_B.

F. Two-view Thickness Estimation

This section describes the proposed method for estimating $\hat{t}$ of a falling thin particle. The method analyzes the aligned images column-wise to determine which columns better describe the thickness information of the particle. It can only work with particles captured with sideways orientation (orientation *1b*), detected using the method described in Section III-D.

The proposed method for estimating $\hat{t}$ can be divided into six steps: *i*) alignment, *ii*) image projection, *iii*) subpixel thickness analysis, *iv*) edge matching and 3D triangulation, *v*) orientation-based thickness normalization, *vi*) CI

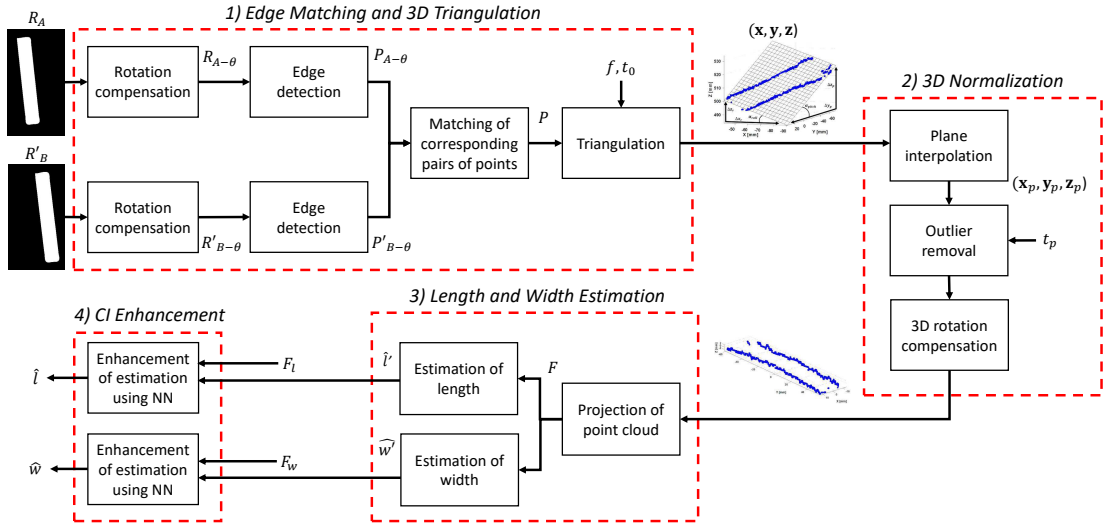

Figure 9. Outline of the 3D edge reconstruction step. The step can be divided into four tasks: *1*) edge matching and 3D triangulation, *2*) 3D normalization, *3*) length and width estimation, *4*) CI enhancement

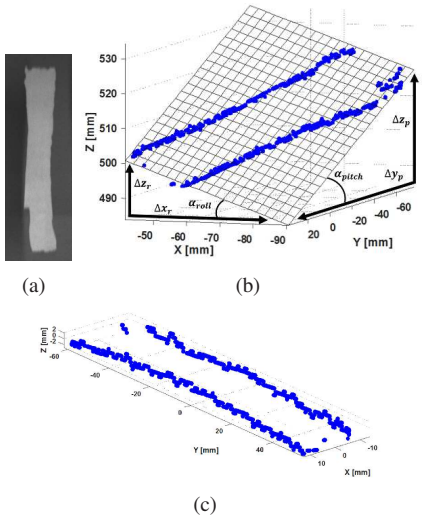

(a) (b)

(c)

Figure 10. Example of a raw material particle (chopped wood strand) and its 3D point cloud: (a) the particle; (b) the 3D point cloud of the edges. The roll and pitch angles α_{roll}, α_{pitch} can be estimated from the fitting plane; (c) the point cloud after compensating for the roll and pitch rotations. The point cloud only contains the 3D coordinates of the edges, since the reconstruction of the surface is not necessary to determine l and w

enhancement. Fig. 11 shows a detailed outline of the two-view thickness estimation step.

1) Alignment: The alignment algorithm uses an ad-hoc procedure to rotate the particle along the y axis of E and enhance the details of the thickness, without introducing artifacts due to interpolation.

The algorithm performs the alignment both on the left and the right border to choose the one that better enhances the thickness.

To align E to the left border, for each row r of R, the algorithm computes the minimum column coordinate $min_c(r)$ belonging to the ROI, and performs a left shift of $s(r) = min_c(r)$ pixels, obtaining the image L_{left}. Similarly, for each row r of R the algorithm computes the maximum column coordinate $max_c(r)$ and performs a right shift of $s(r) = u - max_c(r)$ pixels, where u is the horizontal size of the image, obtaining the image L_{right}.

2) Image Projection: The proposed algorithm projects the image L_{left} on the y axis by computing the projection vector $\mathbf{g}_{left}(c)$ as the mean value of each column c in L_{left}. It applies the same process to L_{right} to obtain the right projection vector $\mathbf{g}_{right}(c)$. To enhance the visibility of the thickness, the final projection vector $\mathbf{g}(c)$ is considered as $\mathbf{g}_{left}$ if $\max_c(\mathbf{g}_{left}(c)) > \max_c(\mathbf{g}_{right}(c))$, otherwise it is considered as $\mathbf{g}_{right}$. If the particle is captured sideways (orientation *1b*), the majority of the incident light is reflected by the thickness, and the projection exhibits a distinct peak in the corresponding columns. On the other hand, in the case of particles captured with a frontal orientation (orientation *1a*), the light is reflected more uniformly by its surface, and no distinct peak is present (Fig. 12).

If a rightward alignment is chosen, the algorithm flips $\mathbf{g}$ horizontally. Then, it extracts from $\mathbf{g}$ the local maxima $\mathbf{m} = [m_1, m_2, \ldots, m_n]$, and selects the peak $m_{max} \in \mathbf{m}$ in the most leftward position, corresponding to the region of L where the thickness is visible. Spurious peaks can be caused by reflections in the central part of the particle and do not correspond to the region of the image in which the thickness is visible. After that, the algorithm extracts the position l_{max} of m_{max}, which corresponds to the center of the thickness of the particle in the aligned image L_A.

Subsequently, the proposed algorithm applies for each row r a reverse shift of $-s(r)$ pixels on the position l_{max} to recover the coordinates $C(x, y)(r)$ of the center of the thickness in the original image E.

3) Sub-pixel Thickness Analysis: The system performs an effective sub-pixel analysis in the projected images, by applying a cubic smoothing spline [10] to $\mathbf{g}$, obtaining a smooth representation G_s with a higher resolution. Then, it calculates the global maximum of the intensity $m_{s,max}$ from G_s and extracts the points in its neighborhood that fulfill $G(r)_s > h_{max} - (p_{max}/2)$, where h_{max} and p_{max} are the height and prominence of the peak $m_{s,max}$, obtaining $G'_s \subset G_s$. The matrix G'_s is the projection corresponding to the region of L

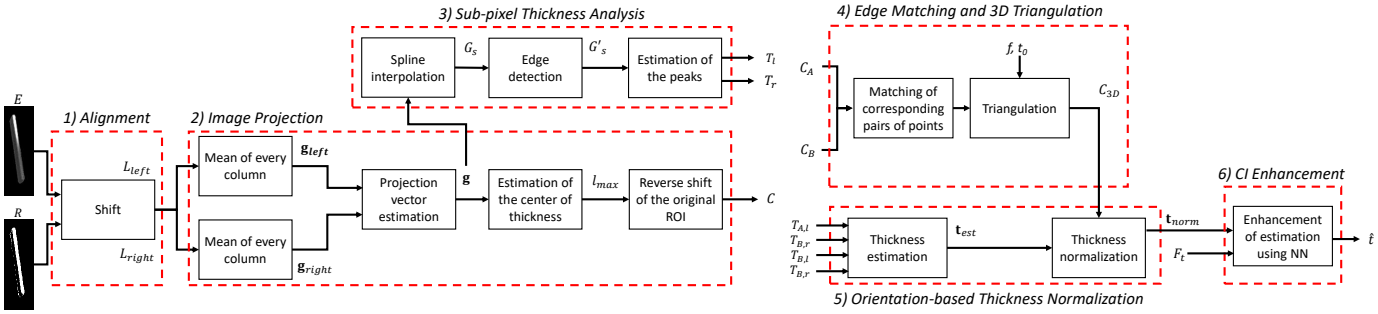

Figure 11. Outline of the two-view thickness estimation step. The step can be divided into six tasks: *1*) alignment, *2*) image projection, *3*) sub-pixel thickness analysis, *4*) edge matching and 3D triangulation, *5*) orientation-based thickness normalization, *6*) CI enhancement

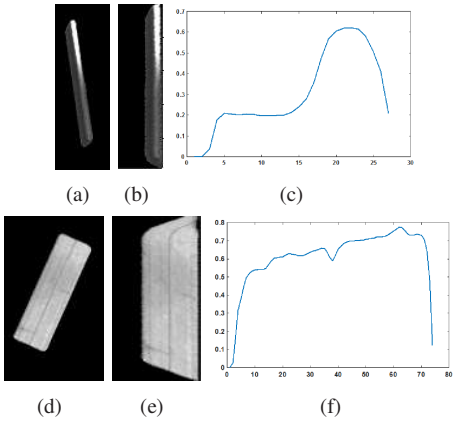

Figure 12. Examples of projections calculated for a calibration parallelepiped: (a) image of a particle E_A, captured sideways; (b) image L_{right} aligned along the y axis; (c) the corresponding projection vector $\mathbf{g}_{right}(c)$ calculated as the mean value of each column of L_{right}; (d,e,f): corresponding images obtained with a particle captured frontally. In the case of a particle captured sideways there is a more distinct peak in the projection in correspondence of the columns of L_{right} where the thickness is visible

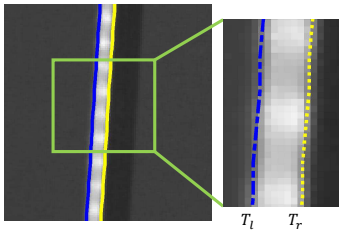

Figure 13. Example of the edges of the thinnest face of the particle T_l, T_r computed using the proposed approach for estimating $\hat{t}$, applied on the calibration parallelepipeds case study

with greater visibility of the thinnest face of the particle.

To estimate which points in G'_s correspond to the edges of the thinnest face of the particle, the algorithm for sub-pixel thickness analysis chooses the edges of the thickness by analyzing the derivative of G'_s. Based on whether L was obtained, with a leftward ($L = L_{left}$) or rightward ($L = L_{right}$) alignment, the left and right position e_l, e_r of the edge are defined as:

$$e_l = \begin{cases} u - \text{argmin}_x\left(d(G'_s)/dx\right) & \text{if } L = L_{left} \\ \text{argmin}_x\left(G'_s\right) & \text{if } L = L_{right} \end{cases}$$
$$e_r = \begin{cases} \text{argmin}_x\left(d(G'_s)/dx\right) & \text{if } L = L_{left} \\ u - \text{argmin}_x\left(G'_s\right) & \text{if } L = L_{right} \end{cases} . \quad (6)$$

Subsequently, the proposed algorithm applies for each row r a reverse shift of $-s(r)$ on the e_l, e_r positions to recover the T_l, T_r coordinates in E of the left and right edge of the thickness, respectively (Fig. 13).

The alignment, projection, and sub-pixel analysis steps are applied to E_A, R_A and to E'_B, R'_B, obtaining $C_A(x,y)(r), C_B(x,y)(r)$, $T_{A,l}, T_{A,r}$, and $T_{B,l}, T_{B,r}$.

4) Edge Matching and 3D Triangulation: Using the procedure described in Section III-E1, the proposed algorithm matches the points C_A with the points C_B and apply Eq. 3 to compute the 3D point cloud $C_{3D}(x,y,z)(r)$.

5) Orientation-based Thickness Normalization: In the case of particles captured with a sideways orientation, the 3D normalization procedure described in Section III-E may not be reliable, since only a small portion of the particle is visible and it is possible that the left and right borders of the strand are not visible as separated lines in both the images.

The proposed normalization algorithm follows the method described in Section III-D to determine the orientation β of the particle with respect to the cameras. After calculating β, the actual thickness t would be captured by the Camera$_A$ as $t_A = t\sin(\beta)$, and by Camera$_B$ as $t_B = t\sin(\beta - \alpha_C)$ (Fig. 7). The algorithm computes t_A by considering the distance from the coordinates of the edges $T_{A,l}, T_{A,r}$. Similarly, it computes t_B using $T_{B,l}, T_{B,r}$. Then, to estimate the thickness t_{est}, we use the computed β, t_A, and t_B in the following equation system:

$$\begin{cases} t_A = t_{est}\sin(\beta) \\ t_B = t_{est}\sin(\beta - \alpha_C) \end{cases} \quad \forall r \ . \quad (7)$$

To provide a more robust estimation, Eq. 7 is solved for each row r in R_A and R_B using $\mathbf{t}_A(r), \mathbf{t}_B(r)$. The obtained values $\mathbf{t}_{est}(r)$ represent the estimated thickness of the particle expressed in pixels. To account for the distance of the particle with respect to Camera$_A$, the proposed method normalizes the values as $\mathbf{t}_{norm}(r) = \mathbf{t}_{est}(r)/\mathbf{d_0}(r)$, where $\mathbf{d_0}(r)$ is computed by considering the distance of the points in $C_{3D}(r)$ from the origin of the axes. The average value $\overline{\mathbf{t}_{norm}}$ is considered as the preliminary estimated thickness $\hat{t}'$.

6) CI Enhancement: The proposed system enhances the estimated thickness $\hat{t}'$ using CI techniques as in Section III-E4. The final enhanced thickness $\hat{t}$ of each thin particle is obtained by applying the neural network N_t on the extracted feature set F_t.

The set F_t contains the following features:

$$F_t = \big[\hat{t'}, \sigma_{(\mathbf{t}_{norm})}, \overline{(\mathbf{t}_A)}, \sigma_{(\mathbf{t}_A)}, \overline{(\mathbf{t}_B)}, \sigma_{(\mathbf{t}_B)}, \overline{(\mathbf{t}_{est})}, \sigma_{(\mathbf{t}_{est})}, \overline{(\beta(r))}, \sigma_{(\beta(r))}, \big]. \quad (8)$$

IV. Experimental Study

This section describes the parameters, the collected datasets, and the performed experiments. The experimental study considered three case studies designed in laboratory conditions to simulate real inline factory applications with high numbers of falling particles and presence of dust. First, we evaluated the accuracy of the proposed approach to estimate $\hat{l}$, $\hat{w}$, and $\hat{t}$ of the single particles. Second, we assessed the capability of the proposed system to correctly detect when a particle can be processed (single particle) or not (clusters of overlapping particles). Third, we analyzed the effect of the orientation estimation module. Fourth, we evaluated the performance impact of the CI in enhancing the accuracy of the granulometric estimation. Finally, we analyzed the working range of the proposed method and the sensitivity of the used parameters.

A. Parameters Used in the Proposed Approach

$\text{Dataset}_{\text{Calibration}}$ contains a subset of the images collected for each case study that served as testbed to empirically tune the parameters of the proposed system. The parameters used in the segmentation step are $th_s = 0.018$ and $th_{Area} = 1000$, while the parameter used in the occlusion management step is $th_c = 10,000$. The parameters used in the orientation estimation step are $t_{frontal} = 20°$, $t_{sideways} = 60°$. The parameter used in the 3D normalization step is $t_p = 2$ mm.

The threshold th_s took the value that permitted the best separation of the multimodal distributions in the images considered in the case studies. The parameter th_{Area} took the value permitting to robustly discard dust and broken particles in the databases considered in the study. This value can be tuned according to preferences and the application scenario. The parameter th_c took the value corresponding to the best performance in detecting occluded particles, after applying the experimental procedure described in Section IV-D. The tested values were in the range $[0, u \times v]$, with step $t_{step} = 1000$, where u and v represent the width and height of image I_A. Similarly, $t_{frontal}$ and $t_{sideways}$ took the values that minimized the error of the proposed system, after applying the experimental procedure described in Section IV-E. The tested values range from $0°$ to $90°$ with step $t_{step} = 10$. The parameter t_p took the value that in most cases discarded all the outliers, while removing only a small percentage of the real points in the point cloud $(\mathbf{x}, \mathbf{y}, \mathbf{z})$. This parameter avoids the presence of outliers, which would influence the resulting granulometry estimation in most cases. On the other hand, removing some of the real points would still allow to perform a correct estimation.

B. Collected Datasets: Three Case Studies

The system captured particles falling without constraints in front of the cameras. To simulate a random falling phenomenon, for each acquisition the particles fell from different starting positions.

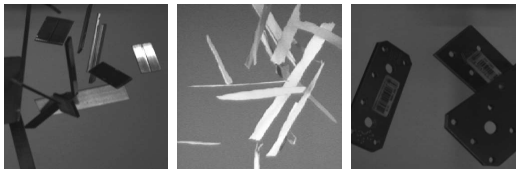

(a) (b) (c)

Figure 14. Examples of particles used in the different case studies: (a) calibration particles; (b) raw particles; (c) manufactured particles

1) Case Study I: Calibration Parallelepipeds: This case study is a testbed to validate the measurement accuracy of the proposed approach. Specifically, it consists of the analysis of images acquired from thin metal particles made of aluminum with known l, w, and t. In particular, the particles are parallelepipeds with regular sides and smooth texture. Fig. 14a shows examples of these particles. The set is composed of 9 particles with size reported in Table II. This case study includes the following database:

- *CSI-A* contains 200 pairs of images per particle, 100 frontal and 100 sideways, for a total of 1800 two-view acquisitions. This database permits to validate the accuracy of our approach in estimating the particle size.

A human supervisor measured the particles using calipers, following the standard measurement procedure [34].

2) Case Study II: Raw Materials: The second case study intends to evaluate the accuracy in estimating the size of raw materials with irregular shape and color. In particular, the particles are chopped pieces of wood, known as strands (Fig. 14b), used in the production of Oriented Strand Boards (OSB). OSBs are engineered wood panels widely adopted in manufacturing, construction, and logistics. The granulometry of the strands has a great effect on the quality, cost and environmental impact of the produced panels [35]. This case study includes two image databases:

- *CSII-A* is composed of two typologies of particles, representative of different working conditions in a real plant. The database contains pairs of images from 100 particles compliant with the reference size provided by the manufacturing industry, having an average $\overline{l} \times \overline{w} \times \overline{t}$ size of $115 \times 20 \times 0.70$ mm, a minimum size of $78 \times 11 \times 0.3$ mm, and a maximum size of $126 \times 47 \times 1.55$ mm. In addition, it includes pairs of images from 100 particles non-compliant with the reference size (e.g., due to stranding errors or wearing of the transport systems), with an average $\overline{l} \times \overline{w} \times \overline{t}$ size of $91 \times 9 \times 0.65$ mm, a minimum size of $46 \times 3 \times 0.2$ mm, and a maximum size of $122 \times 34 \times 1.85$ mm. To simulate as much as possible a random falling phenomenon, and to be able to compute $\hat{l}$, $\hat{w}$, and $\hat{t}$ of each strand, the particles fell from three types of starting positions: *i*) frontal starting position, *ii*) sideways starting position, and *iii*) starting position intermediate between the frontal and sideways positions. Each particle was acquired separately 8 times for each starting position, for a total of 4800 two-view acquisitions. Database CSII-A is designed to test the accuracy of the granulometric analysis of our approach.
- *CSII-B* contains images of groups of particles. The

Table II
ACCURACY OF THE PROPOSED SYSTEM FOR THE ESTIMATION OF $\hat{l}$, $\hat{w}$, AND $\hat{t}$, APPLIED TO DATABASE CSI-A (CASE STUDY I: CALIBRATION PARALLELEPIPEDS). IN TOTAL, 1800 PAIRS OF IMAGES ARE USED

Real size [mm]			Estimation error (mean_{std}) [mm]		
l	w	t	$\hat{l}$	$\hat{w}$	$\hat{t}$
25.12	7.61	1.51	$0.88_{1.62}$	$2.16_{4.55}$	$0.06_{0.06}$
50.27	7.57	1.51	$0.12_{0.09}$	$1.34_{1.30}$	$0.04_{0.02}$
100.10	7.58	1.54	$0.12_{0.37}$	$0.18_{0.19}$	$0.02_{0.01}$
25.21	15.79	2.01	$0.23_{0.36}$	$0.29_{0.66}$	$0.01_{0.02}$
50.26	15.65	2.00	$0.17_{0.21}$	$0.29_{0.28}$	$0.01_{0.01}$
100.18	15.63	2.00	$0.11_{0.14}$	$0.19_{0.21}$	$0.01_{0.01}$
40.06	25.21	3.04	$0.70_{1.72}$	$4.94_{1.93}$	$0.01_{0.02}$
50.11	39.96	2.97	$0.11_{0.09}$	$2.08_{1.25}$	$0.02_{0.05}$
100.43	39.95	2.97	$0.06_{0.05}$	$0.05_{0.15}$	$0.01_{0.02}$

database is composed of 200 images, with a variable number of particles of different sizes in each image, captured with heterogeneous positions and orientations. This database is used to study the accuracy of the occlusion detection step (Section III-C). A human supervisor labeled each 8-connected component, indicating if it represents a separated particle or overlapping particles. A total of 271 connected components are present in the database.

For each database, a human supervisor measured the particles using calipers, following the standard measurement procedure [34]. However, a measurement uncertainty up to 3 mm is present in l and w. The uncertainty is due to the procedure interpretation, to irregularities of the strand, and to their non-rigid structure. For similar reasons, measurements of t present a measurement uncertainty up to 0.05 mm.

3) Case Study III: Manufactured Products: This case study intends to analyze the performance of the proposed system with particles that should have a certified size, but which may show variations due to the production process. Specifically, this case study analyzes metal plate brackets (Fig. 14c), which constitute a good example of final manufactured products. This case study includes the following database:

- *CSIII* contains 21 objects, with 24 pairs of images per object. The images have been captured with the three types of starting positions, 8 times for each position, for a total of 504 two-view acquisitions. The particles have an average $\overline{l}\times\overline{w}\times\overline{t}$ size of $83\times27\times2.04$ mm, a minimum size of $40\times15\times1.5$ mm, and a maximum size of $120\times40\times2.79$ mm.

A human supervisor measured the particles using calipers, following the standard measurement procedure [34].

C. Accuracy of the Granulometric Estimation

1) Case Study I: Table II shows the accuracy of the proposed system for the granulometric estimation for the database CSI-A. In particular, the table shows the mean and the standard deviation of the estimation error for each particle in the database CSI-A. The obtained results are satisfactory and demonstrate the applicability of the proposed system for many real application conditions. With regard to $\hat{l}$ and $\hat{w}$, in the majority of cases, the mean and standard deviation of the error are < 1 mm. Considering $\hat{t}$, in the majority of cases the mean and standard deviation of the error are < 0.05 mm.

Table III
ACCURACY OF THE PROPOSED SYSTEM FOR DATABASE CSII-A (CASE STUDY II: RAW MATERIALS)

DB	N. imgs	Estimation error (mean_{std}) [mm]		
		$\hat{l}$	$\hat{w}$	$\hat{t}$
CSII-A	4800	$0.98_{0.82}$	$0.80_{1.30}$	$0.10_{0.09}$

Table IV
ACCURACY OF THE PROPOSED SYSTEM FOR DATABASE CSIII (CASE STUDY III: MANUFACTURED PRODUCTS)

DB	N. imgs	Estimation error (mean_{std}) [mm]		
		$\hat{l}$	$\hat{w}$	$\hat{t}$
CSIII	504	$0.40_{0.71}$	$0.11_{0.24}$	$0.07_{0.09}$

2) Case Study II: Table III shows the average error and the corresponding standard deviation for all the particles of the database CSII-A. The obtained errors are slightly higher but comparable with respect to the ones obtained in the case study I, also showing that the proposed system detected particles with an error $\approx 1 \pm 1$ mm for $\hat{l}$ and $\hat{w}$, and with an error $\approx 0.1 \pm 0.1$ mm for $\hat{t}$. These results are satisfactory for real production conditions. Most probably, the error increase with respect to case study I is mainly due to the uncertainty in the reference measurements performed using a caliper.

3) Case Study III: Table IV shows the average error and the corresponding standard deviation on all the particles of the database CSIII. Results show that the proposed system detected particles with an error $\approx 0.4 \pm 0.7$ mm in the estimation of $\hat{l}$, with an error $\approx 0.1 \pm 0.2$ mm in the estimation of $\hat{w}$, and with an error $\approx 0.1 \pm 0.1$ mm in the estimation of $\hat{t}$. Also in this case, the proposed system showed sufficient accuracy for being used in a wide set of real application conditions.

D. Accuracy of the Occlusion Management

The test described in this section uses the database CSII-B to estimate the accuracy the occlusion management module. Table V presents the obtained confusion matrix. It shows that the proposed method can differentiate occluded and non-occluded particles with an accuracy of 96.31%, and illustrates that the system is capable of performing granulometric estimation also in the case of multiple particles falling at the same time.

It could also be possible to detect occluded particles by thresholding the normalized area difference d_i/a_i using the threshold th_c in the range $[0, 1]$. We evaluated this configuration by varying th_c with step 0.05. In this case, the best obtained classification accuracy was slightly inferior, 89.29%, obtained by using $th_c = 0.65$.

E. Accuracy of the Orientation Estimation

The test described in this section uses the databases CSI-A, CSII-A, and CSIII to analyze the accuracy of the orientation detection module. Table VI presents the estimation error of the whole system when the orientation detection is turned on/off, without the CI enhancement step. This table shows that, in all cases, the use of the orientation detection increases the accuracy of the granulometric estimation. Furthermore, the orientation detection was crucial to obtain a reliable estimation of $\hat{t}$.

Table V
ACCURACY OF THE OCCLUSION DETECTION MODULE.

DB	N. imgs			Predicted	
				Separated	Occluded
CSII-B	200	Real	Separated	15.49%	1.84%
			Occluded	1.84%	80.81%

Table VI
ERROR OF THE PROPOSED SYSTEM OBTAINED WITH AND WITHOUT THE ORIENTATION DETECTION MODULE (WITHOUT CI ENHANCEMENT)

DB	Error w/out orientation detect. (mean$_{std}$) [mm]			Error w. orientation detect. (mean$_{std}$) [mm]		
	$\hat{l}$	$\hat{w}$	$\hat{t}$	$\hat{l}$	$\hat{w}$	$\hat{t}$
CSI-A	$3.33_{1.18}$	$2.38_{2.70}$	$8.50_{2.78}$	$3.05_{0.80}$	$1.06_{0.97}$	$0.49_{0.45}$
CSII-A	$7.47_{3.20}$	$1.33_{1.36}$	$7.24_{2.64}$	$6.42_{3.22}$	$1.65_{1.48}$	$1.77_{1.89}$
CSIII	$4.99_{2.17}$	$2.19_{1.80}$	$4.65_{2.88}$	$3.93_{0.76}$	$0.97_{0.93}$	$0.40_{0.31}$

F. Performance of the CI Enhancement

This section analyzes the impact of CI models to reduce the error of the proposed approach. To obtain a fair comparison, the experimental procedure used a 10-fold cross-validation procedure [36], using 8/10 of the data for training, 1/10 for validation, and 1/10 for testing. The testing subset contains a disjoint set of particles with respect to the training and validation subsets, resulting in the CI model being tested on a particle that was not used for its training nor its validation. This work considers CI models based on Feedforward Neural Networks with one input layer, one hidden layer with tan-sigmoidal nodes, and one output layer with a linear node, which can be considered as universal approximators [37]. The training algorithm is the Levenberg-Marquardt back-propagation algorithm, using at most 150 epochs. The number of neurons in the hidden layer is the one that resulted in the lowest estimation error, after trying different values. For each database and for each particle dimension (l/w/t), the system uses a separated neural network.

Table VII presents the results obtained both with and without the use of CI enhancement for the databases CSI-A, CSII-A, and CSIII. The results show that, for each considered database, the CI module decreased the estimation error. The neural networks trained for database CSI-A have hidden layers with 30, 20, and 80 nodes for the l, w, and t dimensions, respectively, while the neural networks trained for database CSII-A have have hidden layers with 20, 80, and 70 nodes. The neural networks trained for database CSIII have hidden layers with 20, 10, and 60 nodes.

Fig. 15 depicts the improvement in the correlation between the estimated granulometry and the real size of the particle, with error bounds computed at a 95% confidence interval, for l, w, and t separately. The presented results show that the correlation always increased with the CI enhancement.

G. Working Range and Sensitivity Analysis

The experimental procedure to estimate the smallest object measurable by the proposed system analyzes the acquisitions of a set of spheres with a diameter ranging from 3 to 11 mm. In particular, all the spheres with diameter $\geq$ 11 mm were correctly detected.

A similar procedure analyzed the images captured from a set of strands smaller than the average size, with l ranging from

Table VII
ERROR OF THE PROPOSED SYSTEM OBTAINED WITH AND WITHOUT THE CI ENHANCEMENT. A 10-FOLD CROSS-VALIDATION PROCEDURE WAS USED TO TEST THE ACCURACY OF THE CI MODEL

DB	Error w/out CI (mean$_{std}$) [mm]			Error w. CI (mean$_{std}$) [mm]		
	$\hat{l}$	$\hat{w}$	$\hat{t}$	$\hat{l}$	$\hat{w}$	$\hat{t}$
CSI-A	$3.05_{0.80}$	$1.06_{0.97}$	$0.49_{0.45}$	$0.09_{0.13}$	$0.93_{1.41}$	$0.01_{0.01}$
CSII-A	$6.42_{3.22}$	$1.65_{1.48}$	$1.77_{1.89}$	$0.98_{0.82}$	$0.80_{1.30}$	$0.10_{0.09}$
CSIII	$3.93_{0.76}$	$0.97_{0.93}$	$0.40_{0.31}$	$0.40_{0.71}$	$0.11_{0.24}$	$0.07_{0.09}$

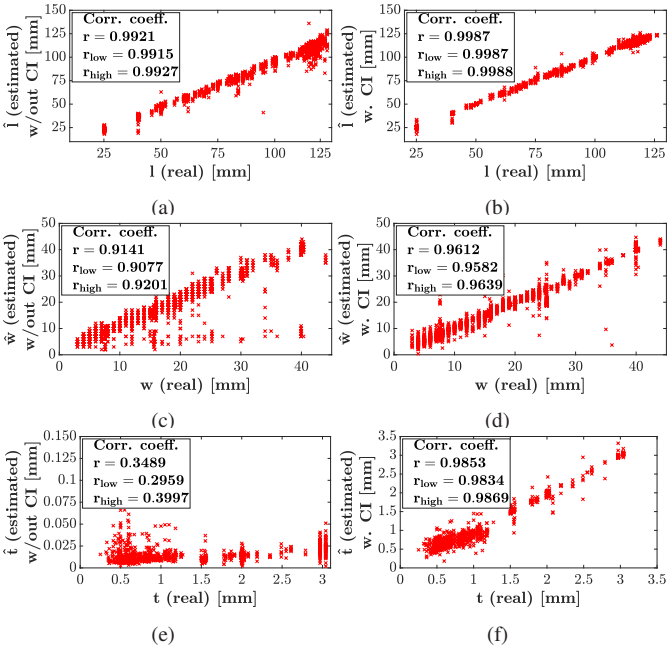

Figure 15. Improvement in the correlation between the estimated and the real size of the particle, with the use of CI enhancement, on aggregated data from databases CSI-A, CSII-A, CSIII: correlation between the estimated and real l, w, and t, without CI (a,c,e) and with CI enhancement (b,d,f). A 10-fold cross-validation was used to test the accuracy of the CI model. The label reports the correlation coefficient r with the corresponding lower and upper bounds r_{low}, r_{high} computed for a 95% confidence interval. Results show the relevant improvement in estimating $\hat{t}$ using CI techniques

13 to 29 mm and with w ranging from 2 to 7 mm, and the strands with $w \geq 6$ mm were correctly detected, as long as the surface of the strand is visible in the cameras. The upper limit of the working range is represented by the acquisition volume, which in the used setup (Fig. 2) is equal to $w_s \times h_s \times d_s = 400 \times 225 \times 500$ mm. Nevertheless, the use of optics with different focal lengths in the acquisition setup would allow the proposed system to analyze particles with different size ranges.

The experimental study also included a sensitivity analysis on the parameters of the proposed approach for the database CSI-A. The obtained results demonstrated that the approach is robust to small variations of the parameters. We varied by $\pm 20\%$ the value of the parameter th_{Area}, obtaining no variation in the mean estimation error of $\hat{l}$, and variations $\leq$ 0.01 mm and $\leq$ 0.04 mm for $\hat{w}$ and $\hat{t}$, respectively. This analysis showed that the most important parameters are the thresholds $th_{frontal}$, $th_{sideways}$, used to decide whether the images should be processed to estimate l, w, or t. The sensitivity analysis considered variations of $\pm 20\%$, and in the worst case, differences in the mean estimation error were

≤ 0.1 mm, ≤ 0.3 mm, ≤ 0.7 mm for l, w, and t, respectively. Furthermore, the sensitivity analysis considered variations of $\pm 20\%$ for the parameter th_c used in the occlusion management step, obtaining in the worst case a classification error of 6%, and showing that the approach would still be able to correctly detect the vast majority of occluded strands.

V. Conclusions

This paper proposed a novel vision system for the inline particle size measurement of falling thin particles, applied with positive results to three case studies, including calibration particles with precise size, raw materials used in the wood engineering industry, and manufactured metal plates. The case studies were designed in laboratory conditions simulating real inline factory conditions, with high numbers of falling particles and presence of dust.

The proposed system is able to compute the length (l), width (w), and thickness (t) of the particles falling with uncontrolled position and orientation. The only requirement is that the particles fall in the fields of view of the cameras. The proposed system obtained estimation errors of ≤ 1 mm (1%), ≤ 1 mm (5%), and ≤ 0.1 mm (4%) in estimating $\hat{l}$, $\hat{w}$, and $\hat{t}$ of the particles, respectively. The system was able to correctly classify and discard overlapping particles, with 4% classification error, and to correctly estimate the orientation of the particles to analyze the corresponding size.

The proposed computational chain is general and the use of optics with different focal lengths in the acquisition setup would allow the proposed system to analyze particles with different size ranges.

The performed tests showed that the system can be successfully applied for the inline monitoring of the granulometry of falling particles, instead of relying on offline sampling-based techniques, which are time-consuming, suffer from a measurement delay, and may not represent the current working point of the plant.

References

[1] A. Jillavenkatesa, L.-S. H. Lum, and S. Dapkunas, "NIST recommended practice guide: particle size characterization," Special Publication (NIST SP)-960-1, Tech. Rep., 2001.

[2] H. G. Merkus, *Particle Size Measurements: Fundamentals, Practice, Quality*, ser. Particle Technology Series. Springer, 2009.

[3] A. Mavilio, M. Fernández, M. Trivi, H. Rabal, and R. Arizaga, "Characterization of a paint drying process through granulometric analysis of speckle dynamic patterns," *Signal Process.*, vol. 90, no. 5, pp. 1623–1630, 2010.

[4] M. Dema, C. Turner, H. Sari-Sarraf, and E. Hequet, "Machine vision system for characterizing horizontal wicking and drying using an infrared camera," *IEEE Trans. on Ind. Inform.*, vol. 12, no. 2, pp. 493–502, 2016.

[5] J. Kozakiewicz, "Image analysis algorithm for detection and measurement of Martian sand grains," *Earth Science Informatics*, January 2018.

[6] S. Ferrari, V. Piuri, and F. Scotti, "Image processing for granulometry analysis via neural networks," in *Proc. of CIMSA*, July 2008, pp. 28–32.

[7] R. Donida Labati, A. Genovese, E. Muñoz, V. Piuri, F. Scotti, and G. Sforza, "Improving OSB wood panel production by vision-based systems for granulometric estimation," in *Proc. of RTSI*, Turin, Italy, September 2015.

[8] W. Wang, "Image analysis of grains from a falling stream," in *Proc. of ICIG*, 2007, pp. 363–367.

[9] R. C. Gonzalez and R. E. Woods, *Digital Image Processing (3^{rd} Edition)*. Upper Saddle River, NJ, USA: Prentice-Hall, Inc., 2006.

[10] C. De Boor, *A practical guide to splines; rev. ed.*, ser. Applied mathematical sciences. Berlin: Springer, 2001.

[11] G. Acampora, V. Loia, M. Nappi, and S. Ricciardi, "Hybrid computational intelligence for ambient intelligent environments," in *Proc. of the AWIC 2005*, 2005, pp. 26–31.

[12] I. Onederra, M. J. Thurley, and A. Catalan, "Measuring blast fragmentation at Esperanza mine using high-resolution 3D laser scanning," *Mining Technology*, vol. 124, no. 1, pp. 34–36, 2015.

[13] F. Ding, M. Benaoudia, P. Bédard, R. Lanouette, C. Lejeune, and P. Gagné, "Wood chip physical quality definition and measurement," Centre de recherche industrielle du Quebec, Canada, Tech. Rep., 2005.

[14] V. Zapater, L. Martínez-Costa, and G. Ayala, "A granulometric analysis of specular microscopy images of human corneal endothelia," *Comput. Vis. Image Und.*, vol. 97, no. 3, pp. 297–314, 2005.

[15] A. Boschetto and V. Giordano, "Powder sampling and characterization by digital image analysis," *Measurement*, vol. 45, no. 5, pp. 1023–1038, 2012.

[16] M. Salehizadeh and M. T. Sadeghi, *Size Distribution Estimation of Stone Fragments via Digital Image Processing*. Springer, 2010, pp. 329–338.

[17] K. C. Williams, W. Chen, S. Weeger, and T. J. Donohue, "Particle shape characterisation and its application to discrete element modelling," *Particuology*, vol. 12, pp. 80–89, 2014.

[18] E. Blotta, A. Bouchet, M. Brun, and V. Ballarin, "Characterization of bio-dynamic speckles through classical and fuzzy mathematical morphology tools," *Signal Process.*, vol. 93, no. 7, pp. 1864–1870, 2013.

[19] T. K. Koh, N. Miles, S. Morgan, and B. Hayes-Gill, "Image segmentation of overlapping particles in automatic size analysis using multi-flash imaging," in *Proc. of WACV*, 2007, pp. 47–47.

[20] A. Ledda, J. Quintelier, P. Samyn, P. De Baets, and W. Philips, "Quantitative image analysis with mathematical morphology," in *Proc. of ProRISC*, 2003, pp. 399–406.

[21] M. G. Ljungqvist, M. E. Nielsen, B. K. Ersbøll, and S. Frosch, "Image analysis of pellet size for a control system in industrial feed production," *PLoS ONE*, vol. 6, no. 10, 2011.

[22] P. Lavoie, D. Ionescu, and E. M. Petriu, "3D object model recovery from 2D images using structured light," *IEEE Trans. on Instrum. and Meas.*, vol. 53, no. 2, pp. 437–443, 2004.

[23] I. Soppela, S. Airaksinen, J. Hatara, H. Räikkönen, O. Antikainen, J. Yliruusi, and N. Sandler, "Rapid particle size measurement using 3D surface imaging," *AAPS PharmSciTech*, vol. 12, no. 2, pp. 476–484, 2011.

[24] S. Chen and Y. F. Li, "Finding optimal focusing distance and edge blur distribution for weakly calibrated 3-D vision," *IEEE Trans. on Ind. Inform.*, vol. 9, no. 3, pp. 1680–1687, 2013.

[25] J.-H. Han and J.-J. Song, "Statistical estimation of blast fragmentation by applying stereophotogrammetry to block piles," *Int. Journal of Rock Mechanics and Mining Sciences*, vol. 68, pp. 150–158, 2014.

[26] M. J. Noy, "The latest in on-line fragmentation measurement-stereo imaging over a conveyor," in *Proc. of FRAGBLAST*, 2006, pp. 61–66.

[27] R. I. Hartley and A. Zisserman, *Multiple view geometry in computer vision*, 2nd ed. Cambridge University Press, 2004.

[28] M. Okutomi and T. Kanade, "A multiple-baseline stereo," *IEEE Trans. on Pattern Analysis and Machine Intelligence*, vol. 15, no. 4, pp. 353–363, April 1993.

[29] Z. Zhang, "A flexible new technique for camera calibration," *IEEE Trans. Pattern Anal. Mach. Intell.*, vol. 22, pp. 1330–1334, November 2000.

[30] J. Kittler and J. Illingworth, "Minimum error thresholding," *Pattern Recogn.*, vol. 19, no. 1, pp. 41–47, 1986.

[31] J. Heikkila and O. Silven, "A four-step camera calibration procedure with implicit image correction," in *Proc. of CVPR*, June 1997, pp. 1106–1112.

[32] F. Pedersini, A. Sarti, and S. Tubaro, "Accurate and simple geometric calibration of multi-camera systems," *Signal Process.*, vol. 77, no. 3, pp. 309–334, 1999.

[33] M. Nielsen, D. C. Slaughter, and C. Gliever, "Vision-based 3D peach tree reconstruction for automated blossom thinning," *IEEE Trans. on Ind. Inform.*, vol. 8, no. 1, pp. 188–196, 2012.

[34] ISO 9276, "Representation of results of particle size analysis," 2014.

[35] V. Piuri and F. Scotti, "Design of an automatic wood types classification system by using fluorescence spectra," *IEEE Trans. Syst., Man, Cybern. C, Appl. Rev.*, vol. 40, no. 3, pp. 358–366, May 2010.

[36] R. O. Duda, P. E. Hart, and D. G. Stork, *Pattern Classification (2nd Edition)*, 2nd ed. Wiley-Interscience, 2001.

[37] K. Hornik, "Approximation capabilities of multilayer feedforward networks," *Neural Networks*, vol. 4, no. 2, pp. 251–257, 1991.